Published in final edited form as:
Photochem Photobiol. 2009 ; 85(1): 21. doi:10.1111/j.1751-1097.2008.00507.x.

Gold nanorods as contrast agents for biological imaging: optical properties, surface conjugation, and photothermal effects†

Ling Tong[1], **Qingshan Wei**[1], **Alexander Wei**[1], and **Ji-Xin Cheng**[1,2]

[1] Department of Chemistry, Purdue University, West Lafayette, IN, 47907

[2] Weldon School of Biomedical Engineering, Purdue University, West Lafayette, IN, 47907

Abstract

Gold nanorods (NRs) have plasmon-resonant absorption and scattering in the near-infrared (NIR) region, making them attractive probes for *in vitro* and *in vivo* imaging. In the cellular environment, NRs can provide scattering contrast for darkfield microscopy, or emit a strong two-photon luminescence (TPL) due to plasmon-enhanced two-photon absorption. NRs have also been employed in biomedical imaging modalities such as optical coherence tomography (OCT) or photoacoustic tomography (PAT). Careful control over surface chemistry enhances the capacity of NRs as biological imaging agents by enabling cell-specific targeting, and by increasing their dispersion stability and circulation lifetimes. NRs can also efficiently convert optical energy into heat, and inflict localized damage to tumor cells. Laser-induced heating of NRs can disrupt cell membrane integrity and homeostasis, resulting in Ca^{2+} influx and the depolymerization of the intracellular actin network. The combination of plasmon-resonant optical properties, intense local photothermal effects, and robust surface chemistry render gold NRs as promising theragnostic agents.

1. Introduction

Plasmon-resonant gold nanostructures (1–5) are of great interest for optical imaging due to their remarkable capacity to absorb and scatter light at visible and near-infrared (NIR) region (6–11). These optical properties depend on nanoparticle size, shape, and dielectric environment (7,12–14), enabling their application as novel imaging and sensing probes (15–21). Gold nanoparticles can also convert optical energy into heat via nonradiative electron relaxation dynamics (22–24), endowing them with intense photothermal properties (25–35). Such localized heating effects can be directed toward the eradication of diseased tissue, providing a noninvasive alternative to surgery (36). Colloidal gold is well known to be biologically inert and has been used *in vivo* since the 1950’s, namely as adjuvants in radiotherapies (37), but the consideration of such nanoparticles as photothermal agents is relatively recent.

Gold nanorods (NRs) are especially attractive for their highly efficient absorption in the NIR region, a spectral window which permits photons to penetrate biological tissues with relatively high transmittivity. NRs with well-defined shapes and sizes are readily synthesized by seeded growth methods (38,39), and their longitudinal plasmon resonances (LPRs) can be finely tuned as a function of aspect ratio. NRs support a larger absorption cross section at NIR frequencies per unit volume than most other nanostructures and have narrower linewidths due to reduced radiative damping effects (40), with consequently higher optothermal conversion efficiencies (23). The LPRs can also support nonlinear optical effects, such as a plasmon-enhanced two-

---

† This invited paper is part of the Series: Applications of Imaging to Biological and Photobiological Systems

Corresponding author: jcheng@purdue.edu (Ji-Xin Cheng).

photon luminescence (TPL) (18,41). Moreover, the LPRs are sensitive to the polarization of the incident excitation; by slightly adjusting the wavelength of a continuous-wave (cw) polarized laser, individual nanorods could be aligned for several minutes in an optical trap (42). These properties give rise to many exciting possibilities to deploy NRs for biological imaging and photothermal therapy, as illustrated in Fig. 1.

In this paper we review recent developments in the application of NRs as multifunctional agents for biological imaging and for targeted photothermal therapies. In Section 2, we summarize various bioconjugation methods and discuss the importance of removing residual cetyltrimethylammonium bromide (CTAB), a cytotoxic surfactant used in NR synthesis. In Section 3, we discuss the optical imaging modalities supported by NRs, with a particular focus on TPL and its application toward *in vitro* and *in vivo* imaging. Lastly, in Section 4 we discuss several examples involving the use of functionalized NRs as photothermal agents for the selective elimination of cancer cells, with insights into the mechanism of photothermolysis.

2. Synthesis and bioconjugation of gold NRs

Gold NRs can be prepared in gram quantities in micellar solutions comprised of CTAB, a cationic surfactant (38,39). While the exact conditions may vary according to recipe, these syntheses are easily reproduced and can yield NRs with stable absorption peaks ranging from visible to NIR wavelengths (see Fig. 2), if care is taken to consume or quench unreacted gold chloride at the end of the synthesis (43). NRs with LPRs in the range of 750–900 nm have lengths on the order of 50 nm, a size compatible with long blood circulation and permeation into tumor sites via their leaky vasculatures. However, cytotoxicity (44) and nonspecific cellular uptake (45) related to the presence of CTAB may result in collateral injury to healthy cells or tissues, and the introduction of improperly passivated NRs to the blood pool will likely result in their rapid clearance. The complete removal of CTAB, followed by a robust method of surface modification, is required to produce stable NR suspensions with long circulation lifetimes and specific targeting to diseased cells.

The critical micelle concentration of CTAB (ca. 1 mM) is much higher than the reported threshold for cytotoxicity ($IC_{50} < 1\ \mu M$), raising some practical challenges for maintaining stable dispersions of NRs (44,46). At least three methods have been reported to reduce the amount of CTAB to below cytotoxic levels without severely compromising dispersion stability. One involves simple surfactant exchange: CTAB can be partitioned into chloroform and gradually exchanged with phosphatidylcholine (PC), resulting in markedly lower cytotoxicity toward HeLa cells (47). A more common approach involves the displacement of CTAB by sterically stabilizing surfactants, particularly nonionic polymers such polyethyleneglycol (PEG) chains terminating in chemisorptive groups such as thiols or dithiocarbamates (9,45, 48). Removal of CTAB in these cases is generally achieved by membrane dialysis, such that PEG-coated NRs are hardly susceptible to nonspecific cell uptake (45). Other polyelectrolytes have recently been examined for their effects on cell uptake and toxicity, some of which are surprisingly biocompatible (49). For detoxification of gold NRs on a larger scale, it has recently been shown that polystyrenesulfonate (PSS) can serve as a mild detergent and enable the removal of CTAB by ultrafiltration and surfactant exchange, to the extent that no significant toxicity is observed at NR concentrations as high as 85 μg/mL (50). In this case, PSS can only serve as an intermediate peptizing agent, as its physisorption to “CTAB-free” NRs is insufficient for maintaining a stable dispersion.

Cytotoxicity issues aside, there are numerous examples of methods for conjugating NRs with biomolecular labels for cell targeting or intracellular delivery, such as folic acid (33,34), antibodies (9,19,31,48,51), and DNA (52,53), introduced by various surface functionalization methods as illustrated in Fig. 3. Several specific examples are discussed in more detail below.

2.1 Antibody conjugated nanorods (Antibody-NRs)

Antibodies, with their variety and ability to combine high affinity with high specificity, have been widely used in the targeted delivery of nanoparticles. Antibodies have been conjugated to NRs using different linkers for applications in multiplex biosensing, cancer cell imaging, and photothermal therapy. Liao *et al.* prepared antibody-NRs using succinimidyl 6-[3′-(2-pyridyldithio)-propionamido]hexanoate (LC-SPDP), a heterobifunctional cross-linking agent (48). LC-SPDP has a disulfide group that can bind to the NR surface upon reductive cleavage, and an NHS ester for linking primary amines with antibodies. Yu and Irudayaraj developed antibody-NRs into multiplex biosensors based on localized surface plasmon resonance shifts, using 11-mercaptoundecanoic acid (MUA) as a linker for protein conjugation (19). Huang *et al.* adsorbed antibodies for epidermal growth factor receptor (anti-EGFR) onto PSS-coated NRs, and used these to selectively identify cancer cells using conventional and darkfield microscopy (31). Anti-EGFR-NRs can also be used as labels for cancer cells, based on their polarized Raman spectral emissions (9) or their intrinsic TPL signals (51). The antibody-NRs have also been used as photothermal agents to selectively damage cancer cells by NIR laser irradiation (31).

2.2 Folate conjugated nanorods (F-NRs)

Folic acid is an ideal candidate for ligand-based targeting, as numerous examples of folate-conjugated drug carriers have been shown to be transported into cells through receptor-mediated endocytosis (54,55). The high-affinity folate receptor is a highly selective tumor marker overexpressed by over 1/3 of human cancer cell lines (56). Folate derivatives with oligoethyleneglycol spacers have been tethered onto NRs by *in situ* dithiocarbamate (DTC) formation, a recently developed method for the robust functionalization of gold surfaces (33, 34,57). The targeted delivery, cellular uptake, and photothermal effects of F-NRs have been studied extensively by TPL imaging, to be further discussed in sections 3 and 4.

2.3 PEG conjugated nanorods (PEG-NRs)

PEG has well-established “stealth” properties that can shield nanoparticles from fouling by serum proteins (opsonization) and can reduce their rate of clearance by the reticuloendothelial system (RES) (58). NRs with PEG coatings can be prepared by chemisorption as described above, resulting in lower cytotoxicity (59) and nonspecific cellular uptake (45), and improved *in vivo* circulation following intravenous injection in murine models (59). Niidome *et al.* compared the biodistribution of CTAB-NRs and PEG-NRs in mice, and found that 30% of the Au from CTAB-NRs was found in the liver 0.5 h after intravenous (*i.v.*) injection. In contrast, PEG-NRs remained in the blood for a much longer period, with 35% of the Au accumulated in the liver after a 72-h period.

2.4 DNA-functionalized NRs

Gold NRs have been coated with DNA with subsequent photothermal desorption upon NIR irradiation, to investigate the potential of phototriggered gene therapy. Yamada and co-workers treated PC-coated NRs with plasmid DNA to form a NR-DNA complex, whose stability was confirmed by electrophoretic mobility in an agarose gel (52). NIR laser pulses at higher power resulted in a shape transformation (melting) of NRs into spheres and subsequent release of DNA. The application of photothermal DNA release for exogenous control of localized gene expression was demonstrated by Chen *et al.*, using a thiolated version of enhanced green fluorescence (EGFP) DNA mixed with gold NRs (53). Internalization of these NR-DNA conjugates by Hela cells with subsequent exposure to femtosecond (fs) NIR laser pulses at low power resulted in both a rod-to-sphere transformation and the release of DNA to the cytoplasm. As a result, GFP expression was specifically observed in cells exposed to local NIR irradiation, thereby demonstrating the potential of using NR-DNA conjugates and NIR irradiation for local gene expression in specific cells with remote control.

3. *In vitro* and *in vivo* imaging with gold NRs

NIR-absorbing NRs have considerable advantages over molecular dyes and fluorophores as contrast agents for NIR imaging applications. First, their linear and nonlinear absorption cross sections are many times greater than organic molecules; second, their photophysical properties are much more robust against photobleaching effects and other forms of optical fatigue under comparable levels of illumination. Here we review several biological imaging modalities based on the NIR absorbing properties of gold NRs, with a special emphasis on TPL as a recently established mode of nonlinear optical imaging.

3.1 Two-photon luminescence

NRs and other plasmon-resonant nanoparticles are readily visualized under darkfield conditions based on their large scattering cross sections (see Section 3.2). However, plasmons can also be used to enhance photophysical processes resulting in luminescence, a fact that is rapidly gaining appreciation. This may seem counterintuitive at first, as gold is well known to quench the emission of nearby fluorophores due to back-electron transfer (60,61). However, gold itself is able to produce a weak photoemission via interband transitions, and can be enhanced by many orders of magnitude when coupled with an appropriate plasmon excitation (62,63). For example, linear photoluminescence from gold NRs can be enhanced by a factor of over a million compared with bulk gold (64), and NRs subjected to pulsed laser excitation are able to emit a strong TPL (18,41,65). The benefits of multiphoton imaging are manifold: (i) multiphoton processes have a nonlinear dependence on excitation intensity and can be resolved in the axial direction to provide three-dimension (3D) spatial resolution; (ii) TPL and other multiphoton processes can be excited at NIR frequencies between 800 and 1300 nm, the window of greatest transmittivity through biological tissue; (iii) the TPL can be spectrally separated from tissue autofluorescence; (iv) the power densities required for TPL imaging are orders of magnitude below the damage threshold of biological tissue. It is abundantly clear that TPL and other multiphoton imaging modalities are well suited for early detection of neoplastic cells and tissues, especially with plasmon-resonant contrast agents such as NRs. Several works have now shown the potential of NRs in cellular and intravital TPL imaging (18,34,45,51), and will be discussed in detail below.

Photoluminescence from noble metals was first reported by Mooradian in 1969 (62). Luminescence is generated in a three-step process: (i) excitation of electrons from the *d*- to the *sp*- band to generate electron-hole pairs, (ii) scattering of electrons and holes on the picosecond (ps) timescale with partial energy transfer to the phonon lattice, and (iii) electron-hole recombination resulting in photoemission. Single-photon luminescence from NRs can be amplified 6–7 orders of magnitude via resonant coupling with localized plasmons, presumably unrelated to the LPR mode (64). TPL from nanostructured gold was first reported by Boyd *et al*. in 1986 (63), but the efficiency of photoemission from the gold film is low. However, Gold NRs, with their LPR peaks tuned to NIR frequencies, are particularly well suited as TPL-based imaging agents. The characteristics and mechanism of TPL have been investigated byboth far-field (18,65) and by near-field (41,66) optical scanning techniques.

3.1.1 TPL analysis by far-field microscopy—The TPL of single NRs has been investigated by Wang *et al*. using a laser-scanning far field microscopy (18). A fs-pulsed Ti:sapphire laser with tunable emission wavelengths was used to generate TPL from NRs dispersed on a glass coverslip. A typical emission spectrum of a single nanorod is shown in Fig. 4a, which was excited by a laser tuned to its LPR peak at 786 nm. The broad emission spectrum in the visible (400–650 nm) region includes the electron-hole recombination near the

X and L symmetry points, which is at 518 nm and 654 nm for bulk fcc gold, respectively (63). The nonlinear nature of the signal was confirmed by correlating luminescence intensity with excitation power as the incident pulse energy was varied between 1 and 2 pJ (18). A quadratic relation of the signal intensity on the excitation power was observed, with slope values of 1.97 and 2.17 for the increasing and decreasing power curves, respectively (Fig. 4b). The laser fluence absorbed by a single nanorod was approximately 15 fJ per pulse, well below the established damage threshold of 60 fJ (7).

To determine the relationship between the TPL and the LPR, the TPL intensity of NRs at different excitation wavelengths was collated with the NR extinction spectrum (Fig. 4c). The excitation spectrum has a peak intensity at 820 nm and is coincident with the LPR band, indicating that the TPL from nanorods can be attributed to their plasmon-enhanced two-photon absorption cross section. This has been confirmed by comparing the TPL intensities of NRs with different plasmon resonance peaks (λ_{max} = 660, 786, and 804 nm) using the same laser excitation source (λ_{ex}=785 nm) (Fig. 4d). The NRs with LPR peaks near the excitation wavelength clearly produce stronger TPL signals than the off-resonant NRs, consistent with a recent study on the TPL characteristics of gold NRs produced by lithographic methods (65).

The TPL intensity of gold NRs is dependent on the polarization of incident excitation, and thus enhanced when the incident field is aligned with the LPR along the nanorod axis. Horizontally and vertically polarized excitations produced TPL signals with the same average brightness, indicating these emissions were generated by individual NRs (e.g. spots 1 and 2, Fig. 5a, b), whereas brighter spots were presumed to be clusters of NRs (e.g. spot 3). All TPL emissions from single NRs were observed to be sensitive to the incident polarization and followed a $\cos^4$ function (Fig. 5c), similar to that established for the two-photon excitation of single fluorescent molecules. This relation further confirms that the TPL signals are generated by a coherent two-photon absorption process. However, the TPL emission from nanorods is essentially depolarized (Fig. 5d), similar to other types of luminescence and second-harmonic generation (67), but in contrast to conventional plasmon-resonant scattering processes which retain most of the incident polarization (17, 40). The depolarization is in accord with the TPL emission generated by electron-hole recombination as originally proposed by Mooradian (62).

3.1.2 TPL analysis by near-field microscopy—TPL from plasmonic nanostructures has also been studied by Okamoto and coworkers (41,66) using scanning near-field optical microscopy (SNOM), revealing complementary information on their emission and polarization characteristics. A typical TPL spectrum of a single NR of submicron dimensions showed two peaks at 650 nm and 550 nm, which were close to the theoretical values (630 nm and 520 nm) based on the energy of electron-hole recombination near the X and L symmetry points of the Brillouin zone, corresponding respectively to the (001) and (111) lattice planes in the gold crystal (66). The photoluminescence lifetime ranged from 0.8 to 2 ns, depending on the size and shape of the particles and the detection wavelength. The relatively long lifetime indicated the photoluminescence was emitted by the recombination of excited electron-hole pairs located very close to the Fermi surface.

A polarization-dependent study of photoluminescence intensity on both incident excitation and near-field emission revealed a $\cos^2$ dependence, which was explained by presenting the two-photon excitation as a pair of sequential one-photon processes (41). Initially, an electron in the *sp* conduction band is excited by the first photon from below the Fermi surface to above it via an intraband transition, resulting in a charge-separated state within the conduction band. A second photon excites an electron from the *d*- band to the *sp*-band, transferring the hole to the *d*- band. Eventually, an electron-hole recombination event results in luminescence. The first transition is resonant with photons polarized along the nanorod axis but the polarization information is rapidly lost after excitation, whereas the second transition is polarization-insensitive. The emission was also found to be independent from the polarization of the incident field, same as that observed by far-field microscopy. Therefore, the photoluminescence polarization follows a $\cos^2$ dependence, and does not depend on a plasmon-enhanced absorption as is the case of the smaller NRs (18). These observations are not in conflict because the submicron NRs used in the near-field study do not have the appropriate aspect ratio to support a dipolar plasmon resonance at NIR frequencies (7,14).

SNOM imaging enables the TPL from the longer gold NRs to be characterized with high spatial resolution, and revealed the intensities to be strongest at the ends (68). This has been attributed to the so-called “lightning rod” effect, in which the local electric field is greatly intensified by its confinement at the NR tip. In addition, a characteristic oscillating pattern was observed and attributed to periodic amplitude modulations of the wave functions for standing-wave plasmon modes (41,66). These features correspond well with calculated local-density-of-state (LDOS) maps: by comparing the NSOM images of NRs having various lengths but similar diameters, the number of oscillations increases with the aspect ratio while the plasmon wave vector is essentially constant, producing a well-defined dispersion relation (69). The influence of the excitation wavelength on the TPL intensity produced by submicron NRs further supports standing-wave plasmon modes as the basis for the observed spatial modulations.

3.1.3 *In vitro* TPL imaging of cultured cells with gold NRs—TPL imaging has proven to be useful for characterizing cellular uptake of gold NRs. One such study involves the targeted delivery of F-NRs to KB cells (a tumor cell line derived from human oral epithelium) overexpressing the high-affinity folate receptor, which is known to internalize folic acid conjugates by receptor-mediated endocytosis (Fig. 6a) (34). F-NRs were incubated with KB cells for 6 h prior to TPL imaging, which revealed them to be present in high density on the surface of the outer membrane (Fig. 6b); in contrast, F-NRs incubated with NIH/3T3 fibroblast cells for a comparable period resulted in little or no labeling (Fig. 6c). F-NR uptake by KB cells was found to be relatively slow: complete internalization was observed after incubation for 17 h, with the F-NRs localized around the perinuclear region (Fig. 6d). The linescan intensity in Fig. 6d illustrates the high signal-to-background ratio of the TPL contrast generated by internalized nanorods (Fig. 6e). The intracellular migration of F-NRs was further characterized by single-particle tracking analysis and exhibited a bidirectional motion between the nucleus and the plasma membrane, suggestive of directed transport along microtubules (34).

The issue of nonspecific cellular uptake using NRs with different surface coatings has also been investigated by TPL microscopy (45). Nonspecific uptake is a critical issue which must be addressed prior to clinical applications of NRs and other types of nanoparticles. NRs coated with CTAB, bis(*p*-sulfonatophenyl)phenylphosphine (BSP), and methylated PEG (introduced by *in situ* DTC formation) were incubated with KB cells for a 24-h period, then washed and evaluated for TPL signal intensities. The highest levels of nonspecific cell uptake were observed with CTAB-NRs, presumably due to the fusogenic nature of the cationic CTAB. Appreciable uptake was also observed with the anionic BSP coating, but was greatly reduced in the case of mPEG-NRs (*ca*. 6% relative to CTAB-NRs).

In vitro TPL imaging with NRs has also been performed in 3D, using cancer cells supported in a collagen matrix to mimic epithelial tissue (51). EGFR-overexpressing A431 skin cancer cells were labeled with anti-EGFR-conjugated NRs, which could be imaged with a penetration depth of 75 μm using 60 times less laser power than that needed to induce two-photon autofluorescence (TPAF) from cellular components. Consequently, the TPL from NRs was 3 orders of magnitude brighter than the background TPAF emission, and no damage to the tissue phantom was observed.

3.1.4 *In vivo* TPL imaging with gold NRs—

TPL imaging provides high 3D spatial resolution and sufficient penetration depth to monitor biological events *in vivo*. Wang *et al*. provided the first demonstration of intravital TPL imaging by monitoring NRs flowing through the blood vessels in a mouse earlobe (18). Picomolar concentrations of CTAB-NRs were introduced by tail vein injection, and then presumably diluted in the blood pool to femtomolar levels prior to real-time TPL imaging (Fig. 5). The TPL signals were approximately three times higher than the background autofluorescence, and the uniform intensities of the emissions in the single-frame image suggest that most of these were generated by single NRs (Fig. 5d). No TPL signals were detected 30 min after injection, indicating the clearance of CTAB-NRs from circulation. However, we and others have observed that PEG-NRs have much longer circulation times, with a half-life on the order of several hours (59).

3.2 Darkfield microscopy

Optical microscopies and imaging modalities based on resonant light scattering remain highly popular, fueled by the continuous developments in detector sensitivity and optical resolving power. Darkfield microscopy is a particularly versatile method for imaging biological samples: although the extinction cross section of gold NRs is dominated by absorption, the amount of scattering produced is more than sufficient for single-particle detection against a dark background (40). In principle, resonant scattering at NIR wavelengths (ca. 800 nm) should provide the maximum reduction in background Rayleigh scattering. Ironically, many of the studies discussed below do not employ the stronger NIR resonance of NRs, because the transverse plasmon mode provides sufficient scattering intensity at the more convenient visible wavelengths.

Gold NRs have proven to be useful contrast agents for cellular imaging by darkfield microscopy (70). For example, antibody-labeled NRs can selectively label malignant carcinoma cell lines in the presence of normal human keratinocytes, by recognition of their cell-surface EGFRs (31). This approach has also been used to monitor the targeted delivery of NRs conjugated with transferrin or cell-penetrating peptides (71,72). Darkfield microscopy can support multiplex labeling strategies, as demonstrated by the simultaneous detection of NRs with different aspect ratios, targeted toward separate cell-surface biomarkers on human breast epithelial cells (73). Darkfield imaging can even be used to measure tissue properties: submicron-length NRs were embedded in a cardiac fibroblast network to track local deformations induced by mechanical stress in real time (74,75).

3.3 Optical coherence tomography

Optical coherence tomography (OCT) is relatively recent modality for biomedical imaging, with depth penetrations in the low millimeter range, axial resolutions on the order of 10 μm, and lateral resolutions in the low micron range (76,77). OCT is noninvasive and analogous in several respects to ultrasound imaging, except that reflections of NIR light are detected rather than sound. This means that OCT can image cellular and even subcellular structures, with 10–25 times greater spatial resolution than that produced by ultrasound imaging, and up to 100 times better than MRI or CT (78). Recent technological advances have made it possible to use OCT to image nontransparent tissues, with application toward a broad range of medical needs.

OCT typically generates images based on morphology-dependent scattering, but can also do so by differential absorption contrast (spectroscopic mode) or by differences in absorption-scattering profiles. OCT methods based on modulations in optical absorption or scattering can benefit significantly from NIR-active contrast agents such as gold NRs (79,80). However, the mode of contrast generation should be considered: while NRs have been employed in conventional backscattering OCT, their optical response is dominated by absorption, so a very high concentration would be required to produce detectable contrast (79). NIR-absorbing NRs are much better suited to support OCT modalities based on differential absorption or backscattering albedo (the ratio of backscattering to total extinction), which have the advantage of producing contrast in tissues with intrinsically high scattering cross sections. This has been demonstrated with NRs in highly backscattering tissue phantoms, with an estimated detection limit as low as 30 ppm (79). The narrow absorption linewidths of gold NRs can also be used to enhance a spectroscopic mode of OCT, and was recently investigated for producing contrast in an excised sample of human breast invasive ductal carcinoma (81). While the polarization-dependent extinction of gold NRs has not yet been exploited for OCT imaging, this parameter may also provide another mechanism for contrast generation by absorption-based modalities.

3.4 Photoacoustic tomography

Gold NRs also support optoacoustic properties that originate from photoinduced cavitation effects. The cavitation process begins on the subpico second timescale with the thermalization of conduction electrons, followed immediately with electron–phonon interactions and temperature increases of hundreds or even thousands of degrees (82). This superheating results in plasma formation and microbubble expansion, followed by its collapse with an acoustic shockwave (83). The expansion and collapse of cavitation bubbles occur on a microsecond timescale, and are easily detected by ultrasonic transducers.

Photoacoustic tomography (PAT) is an emerging noninvasive imaging technique based on NIR-induced photoacoustic effects (84). PAT combines NIR absorption with acoustic detection, providing much higher spatial resolution than pure ultrasonic imaging: laser pulses probe biological structures with micron-scale resolution, as compared with the millimeter resolution of ultrasound waves. However, the low diffusion of propagating acoustic waves permits greater coherence than reflected optical signals, which would be rapidly attenuated by scattering in biological tissue (85). The depth resolution of PAT can be several centimeters in biological tissue, whereas pure optical imaging is limited to depths on the millimeter scale (86,87).

NIR-absorbing gold NRs have recently been employed as contrast agents for PAT, which would otherwise rely on the intrinsic differences in optical absorption within tissue for contrast. PAT images of nude mice were significantly enhanced by the injection of NRs, which could enhance differences in signal intensity with concentration gradients as low as 1.25 pM (Fig. 8) (88). Other examples involving NRs as PAT contrast agents include quantitative flow analysis in biological tissues (89) and the distribution kinetics of drug delivery systems (90).

4. Photothermal effects of gold NRs

The appeal of gold NRs as contrast agents for imaging is amplified exponentially by their additional capability to serve as photothermal agents, with over 96% of the absorbed photons converted into heat by nonradiative processes. NIR irradiation of NRs embedded in polyurethane using a 20 mW laser raised the temperature by over 100 °C within 1 min (23). The *in vitro* photothermal effects of NRs on cultured tumor cells have been reported by a number of groups (31,33,91,92), as well on parasitic protozoans (93), macrophage (94), and bacterial pathogens (95,96). The potential of using NRs for *in vivo* photothermal therapy has recently been demonstrated by Dickerson *et al.*, who exploited the enhanced permeation and retention (EPR) effect for the accumulation of PEG-NRs in tumor xenografts in mice, with partial tumor resorption upon NIR irradiation (97).

Gold NRs exhibit a high optothermal conversion efficiency, with a larger absorption cross section at NIR frequencies per unit volume than most other types of nanostructures (98). The absorption of light energy is essentially instantaneous, and faster than the relaxation processes which mediate its release as heat. While initial photon absorption rates are on the fs timescale, the electron-phonon transition is on the order of a few ps, and heat diffusion to the surrounding media generally requires tens to hundreds of ps (82). At low powers or photon densities, heat diffusion is efficient and the result is a measurable increase in temperature, in accord with the widely appreciated concept of local hyperthermia. At high photon densities, the repetitive absorption of photons by gold NRs can exceed the rate of heat diffusion and lead to an extremely rapid rise in local temperature and superheating, resulting in cavitation effects (cf. Section 3.4). We attempt to differentiate these two different mechanisms below, both of which lead to cell injury and death but with potentially different phenotypes.

Localized heating is generally considered the primary mechanism of photoactivated injury inflicted by gold NRs (31,33,34,91,92,94,95) and other plasmon-resonant particles (25–27, 32,35,99). Aqueous suspensions of NRs irradiated at plasmon resonance have been examined by IR thermography, and observed to raise the solution temperature by 26 degrees in 5 min when irradiated at just 20 mW of laser power (23). Huang *et al*. reported the first example of using antibody-NRs to kill cancer cells by widefield NIR irradiation (31). Malignant HSC and HOC cells (derived from human squamous cell carcinoma) overexpressing the EGF receptor were cultured with nonmalignant HaCaT cells (keratinocytes) and treated with anti-EGFR-NRs, then washed and exposed to a continuous-wave (cw) Ti:sapphire laser at 800 nm for several minutes at variable powers. The malignant tumor cells were densely coated with NRs and killed by photothermolysis at a threshold laser power of 10 W/cm^2, whereas the nonmalignant cells were only sparsely coated with NRs, and succumbed to photothermolysis at 20 mW/cm^2. Huff *et al.* characterized the hyperthermic effect of F-NRs on KB cells at the single-cell level using a scanning laser microscope, and found that KB cells with either internalized or membrane-bound F-NRs were damaged upon 30 seconds of cw-NIR irradiation at an incident power as low as 7.5 mW, corresponding to a fluence of 30 J/cm^2 (33). Affected cells were strongly stained with ethidium bromide (EB) and exhibited a dramatic membrane blebbing response (Fig. 9a–b), whereas KB cells without F-NRs did not experience photothermal damage even at an incident power of 60 mW. In addition, NIH/3T3 cells lacking the folate receptor were not labeled with F-NRs, and did not experience photothermal damage at the highest laser powers used (Fig. 9c–d).

The mechanism of photoactivated cell injury by F-NRs was studied in detail by Tong *et al.* (34). First, it was determined that the subcellular localization of the F-NRs strongly affected their ability to deliver the maximum effect, in accord with other studies involving targeted gold nanoparticle clusters (99). The threshold cw laser power needed to induce membrane blebbing in KB cells with internalized F-NRs was determined to be 60 mW, whereas cells with membrane-bound F-NRs experienced blebbing when exposed to a laser power of 6 mW (a fluence of 24 J/cm^2), a difference of an order of magnitude. Tumor cells with membrane-bound F-NRs were also exposed to fs-pulsed NIR laser irradiation, and experienced bleb formation at a threshold power of 0.75 mW, or a fluence of only 3 J/cm^2.

It was also determined that membrane bleb formation, the most obvious phenotype of KB cell necrosis, is not the direct result of NR-mediated photothermolysis (34). First, fluorescence confocal microscopy using KB cells expressing actin-GFP revealed a gross redistribution of the cytoskeletal infrastructure after NR-labeled cells were exposed to NIR irradiation, with strong correlation to membrane blebbing. This redistribution occurred regardless of the distribution of F-NRs on or within the KB cell, and confirmed the active role of actin depolymerization in the blebbing process. Second, a Ca^{2+}-sensitive dye (Oregon Green) was used to establish evidence of an intracellular calcium increase immediately following photothermolysis, suggesting that membrane blebbing was induced chemically, not thermally. This hypothesis was validated by incubating KB cells with membrane-bound F-NRs in Ca^{2+}-free buffer, and exposing them to NIR laser irradiation (Fig. 10a–b). No membrane blebs or other morphological changes could be observed after laser treatment, but the addition of millimolar $CaCl_2$ resulted immediately in membrane blebbing, with subsequent positive staining by Oregon Green (Fig. 10c).

How do the F-NRs contribute toward the membrane blebbing response? Cavitation effects, promoted by the high photon density intrinsic to confocal laser scanning microscopy, are the most likely reason for the observed downstream response (26,30,83,99–101). Photoacoustic bursts provide the basis for "optoporation" events that can compromise the integrity of the cell membrane, permitting free exchange between intracellular and extracellular space and the disruption of cell homeostasis. In the case of the study above (34), NR-mediated cavitation is presumed to be responsible for the rapid influx of Ca^{2+}, which activates a number of proteases and signaling pathways that contribute toward the degradation of the actin filament network, and ultimately to membrane blebbing.

5. Summary and outlook

NIR-absorbing gold NRs can be used as optical contrast agents in a number of imaging modalities, and are also highly efficient transducers of light energy into heat. The gold NR surface can be functionalized with biomolecular species such as antibodies and folic acid for targeted cell delivery, and considerable progress has been made to remove the cytotoxic surfactant CTAB, which can also interfere with selective cell labeling and uptake. The many examples discussed above illustrate the exciting potential of using functionalized NRs for theragnostics, by coupling biomedical imaging with photothermal therapy to provide a noninvasive alternative to surgery for cancer treatments. Preclinical evaluation of derivative NRs remains an outstanding issue, and additional *in vivo* experiments are needed to test the translation potential of this method. Well-defined surface chemistry will play a vital role in the continued development of NR-based theragnostics, which may one day result in a medical nanotechnology that is potent, selective, and safe.

Acknowledgments

This work was supported in part by an AHA predoctoral fellowship for Ling Tong.

References

1. Murphy CJ, Sau TK, Gole AM, Orendorff CJ, Gao J, Gou L, Hunyadi SE, Li T. Anisotropic metal nanoparticles: synthesis, assembly, and optical applications. J Phys Chem B 2005;109:13857–13870. [PubMed: 16852739]
2. Pérez-Juste J, Pastoriza-Santos I, Liz-Marzán LM, Mulvaney P. Gold nanorods: synthesis, characterization and applications. Coord Chem Rev 2005;249:1870–1901.
3. Hirsch LR, Gobin AM, Lowery AR, Tam F, Drezek RA, Halas NJ, West JL. Metal nanoshells. Annals Biomed Eng 2006;34:15–22.
4. Huang X, Jain PK, El-Sayed IH, El-Sayed MA. Gold nanoparticles: interesting optical properties and recent applications in cancer diagnostics and therapy. Nanomed 2007;2:681–693.
5. Skrabalak SE, Chen J, Sun Y, Lu X, Au L, Cobley CM, Xia Y. Gold nanocages: synthesis, properties, and applications. Acc Chem Res. 2008 in press.
6. Klar T, Perner M, Grosse S, von Plessen G, Spirkl W, Feldmann J. Surface-plasmon resonances in single metallic nanoparticles. Phys Rev Lett 1998;80:4249–4252.
7. El-Sayed MA. Some interesting properties of metals confined in time and nanometer space of different shapes. Acc Chem Res 2001;34:257–264. [PubMed: 11308299]
8. Dulkeith E, Niedereichholz T, Klar TA, Feldmann J. Plasmon emission in photoexcited gold nanoparticles. Phys Rev B 2004;70:205424.
9. Huang X I, El-Sayed H, Qian W, El-Sayed MA. Cancer cells assemble and align gold nanorods conjugated to antibodies to produce highly enhanced, sharp, and polarized surface Raman spectra: a potential cancer diagnostic marker. Nano Lett 2007;7:1591–1597. [PubMed: 17474783]

10. Danckwerts M, Novotny L. Optical frequency mixing at coupled gold nanoparticles. Phys Rev Lett 2007;98:026104. [PubMed: 17358623]
11. Cognet L, Berciaud S, Lasne D, Lounis B. Nonluminescent nano-objects. Anal Chem 2008;80:2289–2294.
12. Sun Y, Xia Y. Increased sensitivity of surface plasmon resonance of gold nanoshells compared to that of gold solid colloids in response to environmental changes. Anal Chem 2002;20:5297–5305. [PubMed: 12403584]
13. Kelly KL, Coronado E, Zhao L, Schatz GC. The optical properties of metal nanoparticles: the influence of size, shape, and dielectric environment. J Phys Chem B 2003;107:668–677.
14. Noguez C. Surface plasmons on metal nanoparticles: the influence of shape and physical environment. J Phys Chem B 2007;111:3806–3819.
15. Sokolov K, Follen M, Aaron J, Pavlova I, Malpica A, Lotan R, Richartz-Kortum R. Real-time vital optical imaging of precancer using anti-epidermal growth factor receptor antibodies conjugated to gold nanoparticles. Cancer Res 2003;63:1999–2004. [PubMed: 12727808]
16. El-Sayed IH, Huang X, El-Sayed MA. Surface plasmon resonance scattering and absorption of anti-EGFR antibody conjugated gold nanoparticles in cancer diagnostics: applications in oral cancer. Nano Lett 2005;5:829–834. [PubMed: 15884879]
17. Sönnichsen C, Alivisatos AP. Gold nanorods as novel nonbleaching plasmon-based orientation sensors for polarized single-particle microscopy. Nano Lett 2005;5:301–304. [PubMed: 15794615]
18. Wang H, Huff TB, Zweifel DA, He W, Low PS, Wei A, Cheng JX. In vitro and in vivo two-photon luminescence imaging of single gold nanorods. Proc Natl Acad Sci USA 2005;102:15752–15756. [PubMed: 16239346]
19. Yu C, Irudayaraj J. Multiplex biosensor using gold nanorods. Anal Chem 2007;79:572–579. [PubMed: 17222022]
20. Murphy CJ, Gole AM, Hunyadi SE, Stone JW, Sisco PN, Alkilany A, Kinard BE, Hankins P. Chemical sensing and imaging with metallic nanorods. Chem Commun 2008;5:544–557.
21. Anker JN, Hall WP, Lyandres O, Shah NC, Zhao J, Van Duyne RP. Biosensing with plasmonic nanosensors. Nat Mater 2008;7:442–453. [PubMed: 18497851]
22. Link S, El-Sayed MA. Shape and size dependence of radiative, non-radiative and photothermal properties of gold nanocrystals. Int Rev Phy Chem 2000;19:409–453.
23. Chou CH, Chen CD, Wang CRC. Highly efficient, wavelength-tunable, gold nanoparticle based optothermal nanoconvertors. J Phys Chem B 2005;109:11135–11138. [PubMed: 16852358]
24. Petrova H, Juste JP, Pastoriza-Santos I, Hartland GV, Liz-Marzan LM, Mulvaney P. On the temperature stability of gold nanorods: comparison between thermal and ultrafast laser-induced heating. Phys Chem Chem Phys 2006;8:814–821. [PubMed: 16482322]
25. Hirsch LR, Stafford RJ, Bankson JA, Sershen SR, Rivera B, Price RE, Hazle JD, Halas NJ, West JL. Nanoshell-mediated near-infrared thermal therapy of tumors under magnetic resonance guidance. Proc Natl Acad Sci USA 2003;100:13549–13554. [PubMed: 14597719]
26. Pitsillides CM, Joe EK, Wei X, Anderson RR, Lin CP. Selective cell targeting with light-absorbing microparticles and nanoparticles. Biophys J 2003;84:4023–4032. [PubMed: 12770906]
27. O’Neal DP, Hirsch LR, Halas NJ, Payne JD, West JL. Photo-terhmal tumor ablation in mice using near infrared-absorbing nanoparticles. Cancer Lett 2004;209:171–176. [PubMed: 15159019]
28. Loo C, Lowery A, West J, Halas N, Drezek R. Immunotargeted nanoshells for integrated cancer imaging and therapy. Nano Lett 2005;5:709–711. [PubMed: 15826113]
29. El-Sayed IH, Huang X, El-Sayed MA. Selective laser photo-thermal therapy of epithelial carcinoma using anti-EGFR antibody conjugated gold nanorparticles. Cancer Lett 2005;239:125–139.
30. Zharov VP, Letfullin RR, Galitovskaya EN. Microbubbles-overlapping mode for laser killing of cancer cells with absorbing nanoparticle clusters. J Phys D 2005;38:2571–2581.
31. Huang X I, El-Sayed H, Qian W, El-Sayed MA. Cancer cell imaging and photothermal therapy in the near-infrared region by using gold nanorods. J Am Chem Soc 2006;128:2115–2120. [PubMed: 16464114]

32. El-Sayed IH, Huang X, El-Sayed MA. Selective laser photo-thermal therapy of epithelial carcinoma using anti-EGFR antibody conjugated gold nanoparticles. Cancer Lett 2006;239:129–135. [PubMed: 16198049]

33. Huff TB, Tong L, Zhao Y, Hansen MN, Cheng JX, Wei A. Hyperthermic effects of gold nanorods on tumor cells. Nanomed 2007;2:125–132.

34. Tong L, Zhao Y, Huff TB, Hansen MN, Wei A, Cheng JX. Gold nanorods medicate tumor cell death by compromising membrane integrity. Adv Mater 2007;19:3136–3141. [PubMed: 19020672]

35. Chen J, Wang D, Xi J, Au L, Siekkinen A, Warsen A, Li ZY, Zhang H, Xia Y, Li X. Immuno gold nanocages with tailored optical properties for targeted photothermal destruction of cancer cells. Nano Lett 2007;7:1318–1322. [PubMed: 17430005]

36. Wust P, Hildebrandt B, Sreenivasa G, Rau B, Gellerman J, Riess H, Felix R, Schlag PM. Hyperthermia in combined treatment of cancer. Lancet Oncol 2002;3:487–497. [PubMed: 12147435]

37. Sherman AI, Ter-Pogossian M. Lymph-node concentration of radioactive colloidal gold following interstitial injection. Cancer 1953;6:1238–1240. [PubMed: 13106841]

38. Nikoobakht B, El-Sayed MA. Preparation and growth mechanism of gold nanorods (NRs) using seed-mediated growth method. Chem Mater 2003;15:1957–1962.

39. Sau TK, Murphy CJ. Seeded high yield synthesis of short Au nanorods in aqueous solution. Langmuir 2004;20:6414–6420. [PubMed: 15248731]

40. Sönnichsen C, Franzl T, Wilk T, von Plessen G, Feldmann J. Drastic reduction of plasmon damping in gold nanorods. Phys Rev Lett 2002;88:077402. [PubMed: 11863939]

41. Imura K, Nagahara T, Okamoto H. Near-field two-photon-induced photoluminescence from single gold nanorods and imaging of plasmon modes. J Phys Chem B 2005;109:13214–13220. [PubMed: 16852648]

42. Pelton M, Liu M, Kim HY, Smith G, Guyot-Sionnest P, Scherer NF. Optical trapping and alignment of single gold nanorods by using plasmon resonances. Opt Lett 2006;31:2075–2077. [PubMed: 16770437]

43. Zweifel DA, Wei A. Sulfide-arrested growth of gold nanorods. Chem Mater 2005;17:4256–4261. [PubMed: 17415410]

44. Cortesi R, Esposito E, Menegatti E, Gambari R, Nastruzzi C. Effect of cationic liposome composition on in vitro cytotoxicity and protective effect on carried DNA. Int J Pharm 1996;139:69–78.

45. Huff TB, Hansen MN, Zhao Y, Cheng JX, Wei A. Controlling the cellular uptake of gold nanorods. Langmuir 2007;23:1596–1599. [PubMed: 17279633]

46. Berr SS. Solvent Isotope effects on alkyltrimethylammonium bromide micelles as a function of alkyl chain length. J Phys Chem 1987;91:4760–4765.

47. Takahashi H, Niidome Y, Niidome T, Kaneko K, Kawasaki H, Yamada S. Modification of gold nanorods using phosphatidylcholine to reduce cytotoxicity. Langmuir 2006;22:2–5. [PubMed: 16378388]

48. Liao H, Hafner JH. Gold nanorod bioconjugation. Chem Mater 2005;17:436–4641.

49. Hauck TS, Ghazani AA, Chan WCW. Assessing the effect of surface chemistry on gold nanorod uptake, toxicity, and gene expression in mammalian cells. Small 2008;4:153–159. [PubMed: 18081130]

50. Leonov, AP.; Zheng, J.; Clogston, JD.; Stern, ST.; Patri, AK.; Wei, A. Detoxification of gold nanorods by treatment with polystyrenesulfonate. Vol. 2. ACS nano; 2008. p. 2481-2488.

51. Durr NJ, Larson T, Smith DK, Korgel BA, Sokolov K, Ben-Yakar A. Two-photon luminescence imaging of cancer cells using molecularly targeted gold nanorods. Nano Lett 2007;7:941–945. [PubMed: 17335272]

52. Takahashi H, Niidome Y, Yamada S. Controlled release of plasmid DNA from gold nanorods induced by pulsed near-infrared light. Chem Commun 2005;17:2247–2249.

53. Chen CC, Lin YP, Wang CW, Tzeng HC, Wu CH, Chen YC, Chen CP, Chen LC, Wu YC. DNA-gold nanorods conjugates for remote control of localized gene expression by near infrared irradiation. J Am Chem Soc 2006;128:3709–3715. [PubMed: 16536544]

54. Leamon CP, Low PS. Delivery of macromolecules into living cells - a method that exploits folate receptor endocytosis. Proc Natl Acad Sci U S A 1991;88:5572–5576. [PubMed: 2062838]

55. Hilgenbrink AR, Low PS. Folate receptor-mediated drug targeting: from therapeutics to diagnostics. J Pharm Sci 2005;94:2135–2146. [PubMed: 16136558]
56. Sudimack J, Lee RJ. Targeted drug delivery via the folate receptor. Adv Drug Deliv Rev 2000;41:147–162. [PubMed: 10699311]
57. Zhao Y, Perez-Segarra W, Shi Q, Wei A. Dithiocarbamate assembly on gold. J Am Chem Soc 2005;127:7328–7329. [PubMed: 15898778]
58. Lasic DD. The “stealth” liposome: a prototypical biomaterial. Chem Rev 1995;95:2601–2628.
59. Niidome T, Yamagata M, Okamoto Y, Akiyama Y, Takahashi H, Kawano T, Katayama Y, Niidome Y. PEG-modified gold nanorods with a stealth character for in vivo applications. J Control Release 2006;114:343–347. [PubMed: 16876898]
60. Demers LM, Mirkin CA, Mucic RC, Reynolds RA, Letsinger RL, Elghanian R, Viswanadham G. A fluorescence-based method for determining the surface coverage and hybridization efficiency of thiol-capped oligonucleotides bound to gold thin films and nanoparticles. Anal Chem 2000;72:5535–5541. [PubMed: 11101228]
61. Tseng WL, Lee KH, Chang HT. Using nile red-adsorbed gold nanoparticles to locate glutathione within erythrocytes. Langmuir 2005;21:10676–10683. [PubMed: 16262336]
62. Mooradian A. Photoluminescence of metals. Phys Rev Lett 1969;22:185–187.
63. Boyd GT, Yu ZH, Shen YR. Photoinduced luminescence from the noble metals and its enhancement on roughened surfaces. Phys Rev B 1986;33:7923–7936.
64. Mohamed MB, Volkov V, Link S, El-Sayed MA. The ‘lightning’ gold nanorods: fluorescence enhancement of over a million compared to the gold metal. Chem Phys Lett 2000;317:517–723.
65. Bouhelier A, Bachelot R, Lerondel G, Kostcheev S, Royer P, Wiederrecht GP. Surface plasmon characteristics of tunable photoluminescence in single gold nanorods. Phys Rev Lett 2005;95:267405. [PubMed: 16486405]
66. Okamoto H, Imura K. Near-field imaging of optical field and plasmon wave functions in metal nanoparticles. J Mater Chem 2006;16:3920–3928.
67. Anceau C, Brasselet S, Zyss J, Gadenne P. Local second-harmonic generation enhancement on gold nanostructures probed by two-photon microscopy. Opt Lett 2003;28:713–715. [PubMed: 12747716]
68. Imura K, Nagahara T, Okamoto H. Plasmon mode imaging of single gold nanorods. J Am Chem Soc 2004;126:12730–12731. [PubMed: 15469240]
69. Schider G, Krenn JR, Hohenau A, Ditlbacher H, Leitner A, Aussenegg FR, Schaich WL, Puscasu I, Monacelli B, Boreman G. Plasmon dispersion relation of Au and Ag nanowires. Phys Rev B 2003;68:155427.
70. Murphy CJ, Gole AM, Stone JW, Sisco PN, Alkilany AM, Goldsmith EC, Baxter SC. Gold nanoparticles in biology: beyond toxicity to cellular imaging. Acc Chem Res. 2008 in press.
71. Oyelere AK, Chen PC, Huang X, El-Sayed IH, El-Sayed MA. Peptide-conjugated gold nanorods for nuclear targeting. Bioconjug Chem 2007;18:1490–1497. [PubMed: 17630680]
72. Ding H, Yong KT, Roy I, Pudavar HE, Law WC, Bergey EJ, Prasad PN. Gold nanorods coated with multilayer polyelectrolyte as contrast agents for multimodal imaging. J Phys Chem C 2007;111:12552–12557.
73. Yu C, Nakshatri H, Irudayaraj J. Identity profiling of cell surface markers by multiplex gold nanorod probes. Nano Lett 2007;7:2300–2306. [PubMed: 17602538]
74. Orendorff CJ, Baxter SC, Goldsmith EC, Murphy CJ. Light scattering from gold nanorods: tracking material deformation. Nanotechnology 2005;16:2601–2605.
75. Stone JW, Sisco PN, Goldsmith EC, Baxter SC, Murphy CJ. Using gold nanorods to probe cell-induced collagen deformation. Nano Lett 2007;7:116–119. [PubMed: 17212449]
76. Fujimoto JG, Brezinski ME, Tearney GJ, Boppart SA, Bouma B, Hee MR, Southern JF, Swanson EA. Optical biopsy and imaging using optical coherence tomography. Nat Med 1995;1:970–972. [PubMed: 7585229]
77. Zysk AM, Nguyen FT, Oldenburg AL, Marks DL, Boppart SA. Optical coherence tomography: a review of clinical development from bench to bedside. J Biomed Opt 2007;12:051403. [PubMed: 17994864]

78. Fujimoto JG. Optical coherence tomography for ultrahigh resolution in vivo imaging. Nat Biotech 2003;21:1361–1367.

79. Oldenburg AL, Hansen MN, Zweifel DA, Wei A, Boppart SA. Plasmon-resonant gold nanorods as low backscattering albedo contrast agents for optical coherence tomography. Opt Express 2006;14:6724–6738. [PubMed: 19516854]

80. Troutman TS, Barton JK, Romanowski M. Optical coherence tomography with plasmon resonant nanorods of gold. Opt Lett 2007;32:1438–1440. [PubMed: 17546147]

81. Oldenburg AL, Hansen MN, Wei A, Boppart SA. Plasmon-resonant gold nanorods provide spectroscopic OCT contrast in excised human breast tumors. Proceedings of the SPIE 2008;6867:68670E.

82. Link S, Burda C, Mohamed MB, Nikoobakht B, El-Sayed MA. Femtosecond transient-absorption dynamics of colloidal gold nanorods: shape independence of the electron-phonon relaxation time. Phys Rev B 2000;61:6086.

83. Kotaidis V, Plech A. Cavitation dynamics on the nanoscale. Appl Phys Lett 2005;87:213102.

84. Sun T, Diebold GJ. Generation of ultrasonic waves from a layered photoacoustic source. Nature 1992;355:806–808.

85. Wang X, Pang Y, Ku G, Xie X, Stoica G, Wang LV. Noninvasive laser-induced photoacoustic tomography for structural and functional in vivo imaging of the brain. Nat Biotech 2003;21:803–806.

86. Ku G, Wang LV. Deeply penetrating photoacoustic tomography in biological tissues enhanced with an optical contrast agent. Opt Lett 2005;30:507–509. [PubMed: 15789718]

87. Zhang HF, Maslov K, Stoica G, Wang LV. Functional photoacoustic microscopy for high-resolution and noninvasive in vivo imaging. Nat Biotech 2006;24:848–851.

88. Eghtedari M, Oraevsky A, Copland JA, Kotov NA, Conjusteau A, Motamedi M. High sensitivity of in vivo detection of gold nanorods using a laser optoacoustic imaging system. Nano Lett 2007;7:1914–1918. [PubMed: 17570730]

89. Liao CK, Huang SW, Wei CW, Li PC. Nanorod-based flow estimation using a high-frame-rate photoacoustic imaging system. J Biomed Opt 2007;12:064006–064009. [PubMed: 18163822]

90. Chamberland DL, Agarwal A, Kotov N, Fowlkes JB, Carson PL, Wang X. Photoacoustic tomography of joints aided by an etanercept-conjugated gold nanoparticle contrast agent-an ex vivo preliminary rat study. Nanotechnology 2008;19:095101.

91. Takahashi H, Niidome T, Nariai A, Niidome Y, Yamada S. Gold nanorod-sensitized cell death: microscopic observation of single living cells irradiated by pulsed near-infrared laser light in the presence of gold nanorods. Chem Lett 2006;35:500–501.

92. Black KC, Kirkpatrick ND, Troutman TS, Xu L, Vagner J, Gillies RJ, Barton JK, Utzinger U, Romanowski M. Gold nanorods targeted to delta opioid receptor: plasmon-resonant contrast and photothermal agents. Mol Imaging 2008;7:50–57. [PubMed: 18384724]

93. Pissuwan D, Valenzuela SM, Miller CM, Cortie MB. A golden bullet? selective targeting of toxoplasma gondii tachyzoites using antibody-functionalized gold nanorods. Nano Lett 2007;7:3808–3812. [PubMed: 18034505]

94. Pissuwan D, Valenzuela SM, Killingsworth MC, Xu X, Cortie MB. Targeted destruction of murine macrophage cells with bioconjugated gold nanorods. J Nanoparticle Res 2007;9:1109–1124.

95. Norman RS, Stone JW, Gole A, Murphy CJ, Sabo-Attwood TL. Targeted photothermal lysis of the pathogenic bacteria, pseudomonas aeruginosa, with gold nanorods. Nano Lett 2008;8:302–306. [PubMed: 18062714]

96. He W, Henne WA, Wei Q, Zhao Y, Doorneweerd DD, Cheng J-X, Low PS, Wei A. Two-photon luminescence imaging of bacillus spores using peptide-functionalized gold nanorods. Nano Res 2008;1:450–456. [PubMed: 20098661]

97. Dickerson EB, Dreaden EC, Huang X, El-Sayed IH, Chu H, Pushpanketh S, McDonald JF, El-Sayed MA. Gold nanorod assisted near-infrared plasmonic photothermal therapy (PPTT) of squamous cell carcinoma in mice. Cancer Lett 2008;269:57–66. [PubMed: 18541363]

98. Jain PK, Lee KS, El-Sayed IH, El-Sayed MA. Calculated absorption and scattering properties of gold nanoparticles of different size, shape, and composition: applications in biological imaging and biomedicine. J Phys Chem B 2006;110:7238–7248. [PubMed: 16599493]

99. Zharov VP, Galitovskaya EN, Johnson C, Kelly T. Synergistic enhancement of selective nanophotothermolysis with gold nanoclusters: potential for cancer therapy. Lasers Surg Med 2005;37:219–226. [PubMed: 16175635]

100. Yao CP, Rahmanzadeh R, Endl E, Zhang ZX, Gerdes J, Hüttmann G. Elevation of plasma membrane permeability by laser irradiation of selectively bound nanoparticles. J Biomed Opt 2005;10:064012. [PubMed: 16409077]

101. Lapotko DO, Lukianova E, Oraevsky AA. Selective laser nano-thermolysis of human leukemia cells with microbubbles generated around clusters of gold nanoparticles. Lasers Surg Med 2006;38:631–642. [PubMed: 16736503]

102. Gole A, Murphy CJ. Biotin-streptavidin-induced aggregation of gold nanorods: tuning rod-rod orientation. Langmuir 2005;21:10756–10762. [PubMed: 16262348]

103. Gole A, Murphy CJ. Azide-derivatized gold nanorods: functional materials for “click” chemistry. Langmuir 2008;24:266–272. [PubMed: 18052398]

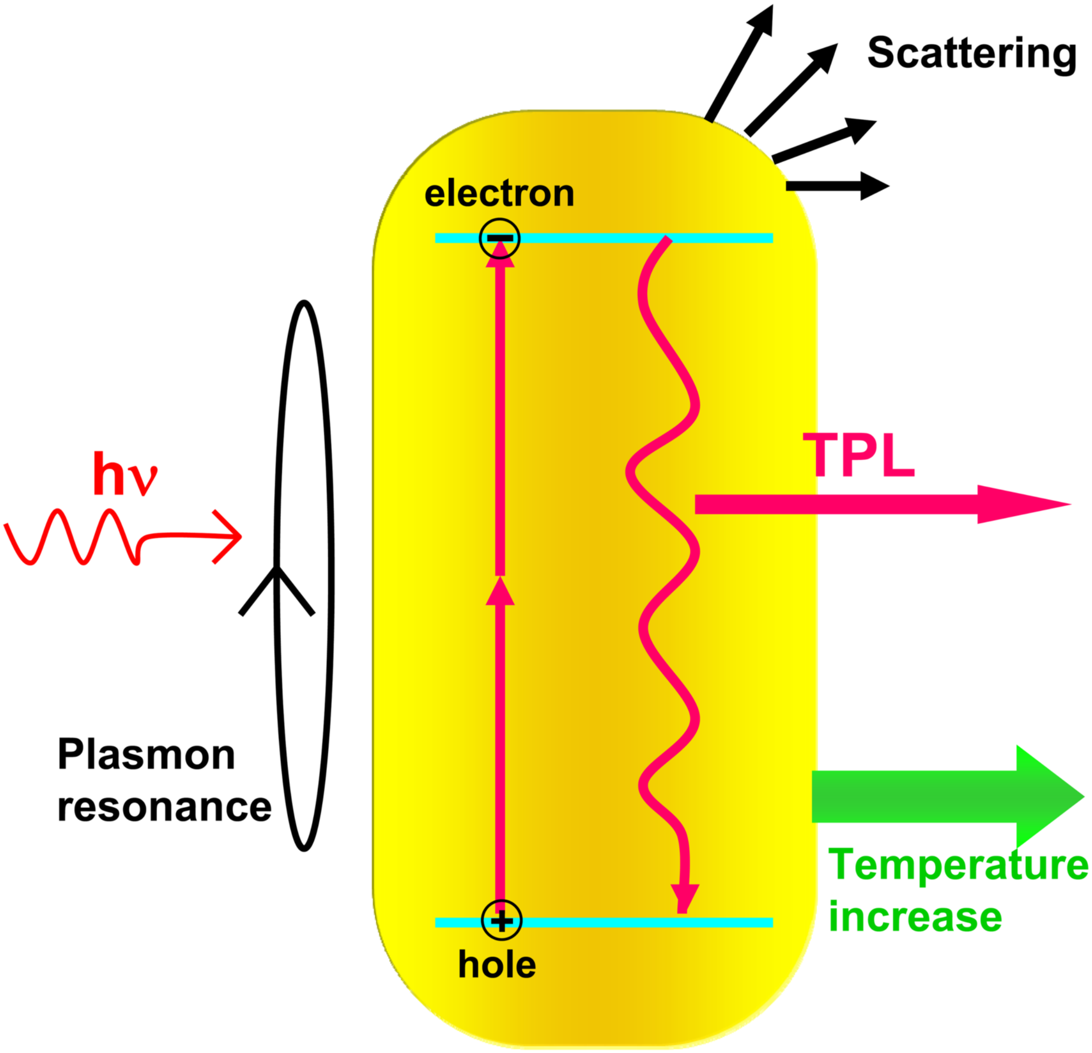

Figure 1. Photophysical processes in gold NRs

NIR irradiation induces the excitation of a LPR mode, resulting mostly in absorption but also some resonant light scattering. An electronic transition from the *d*- band to *sp*- band occurs with two-photon absorption, generating an electron-hole pair; recombination of separated charges results in TPL emission. Heat is also generated as a consequence of electron-phonon collisions.

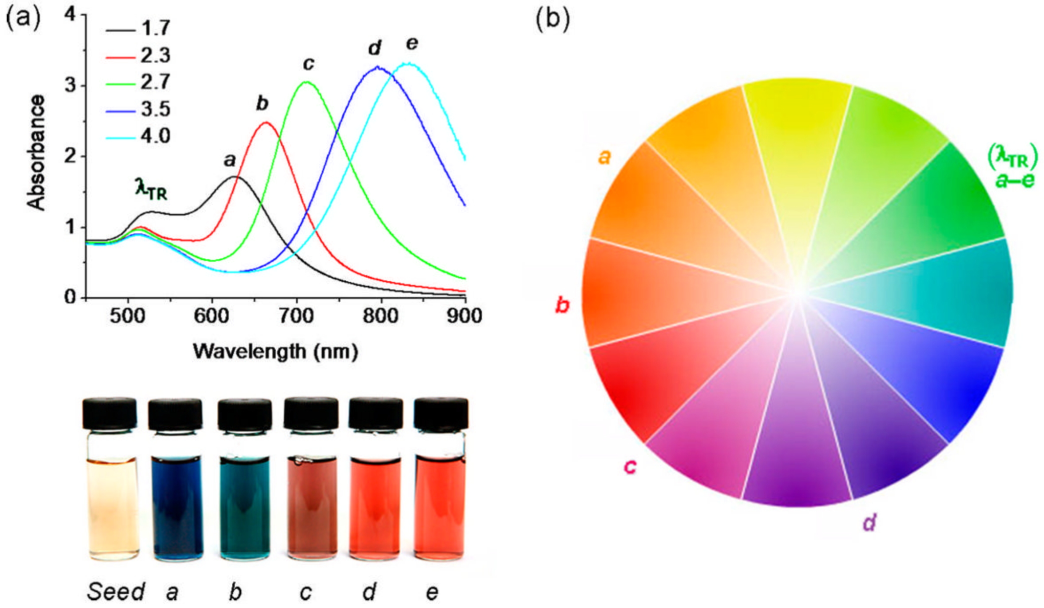

Figure 2. Gold NRs with tunable optical absorptions at visible and NIR wavelengths
(a) Optical absorption spectra of gold NRs with different aspect ratios. (b) Color wheel, with reference to λ_{LR} and λ_{TR} for gold NRs labeled *a*–*e*.

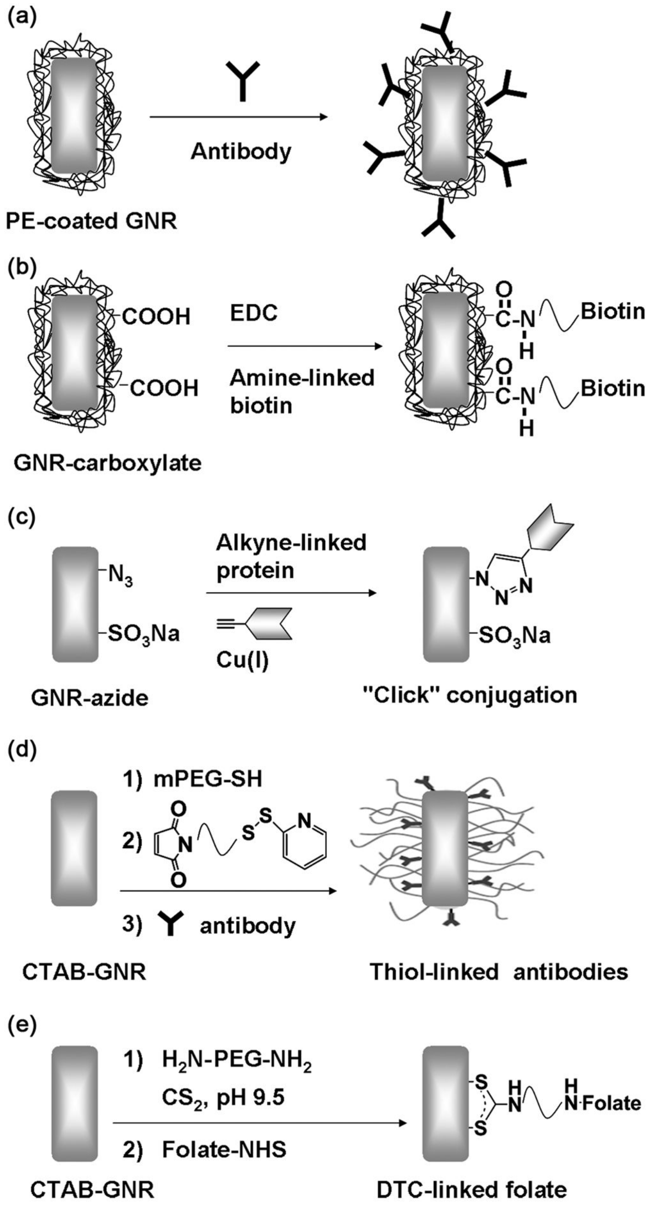

Figure 3. Surface functionalization of gold NRs

(a) Electrostatic adsorption onto polyelectrolyte-coated gold NRs. (b) Conjugation of amine-terminated biotin by carbodiimide coupling (102). (c) Cu-catalyzed “click” addition of alkyne-terminated molecules onto azide-labeled surface (103). (d) Chemisorption of thiolated bioconjugates (48,53,59). (e) Chemisorption of amine-terminated bioconjugates by *in situ* dithiocarbamate (DTC) formation (33,34,45,57).

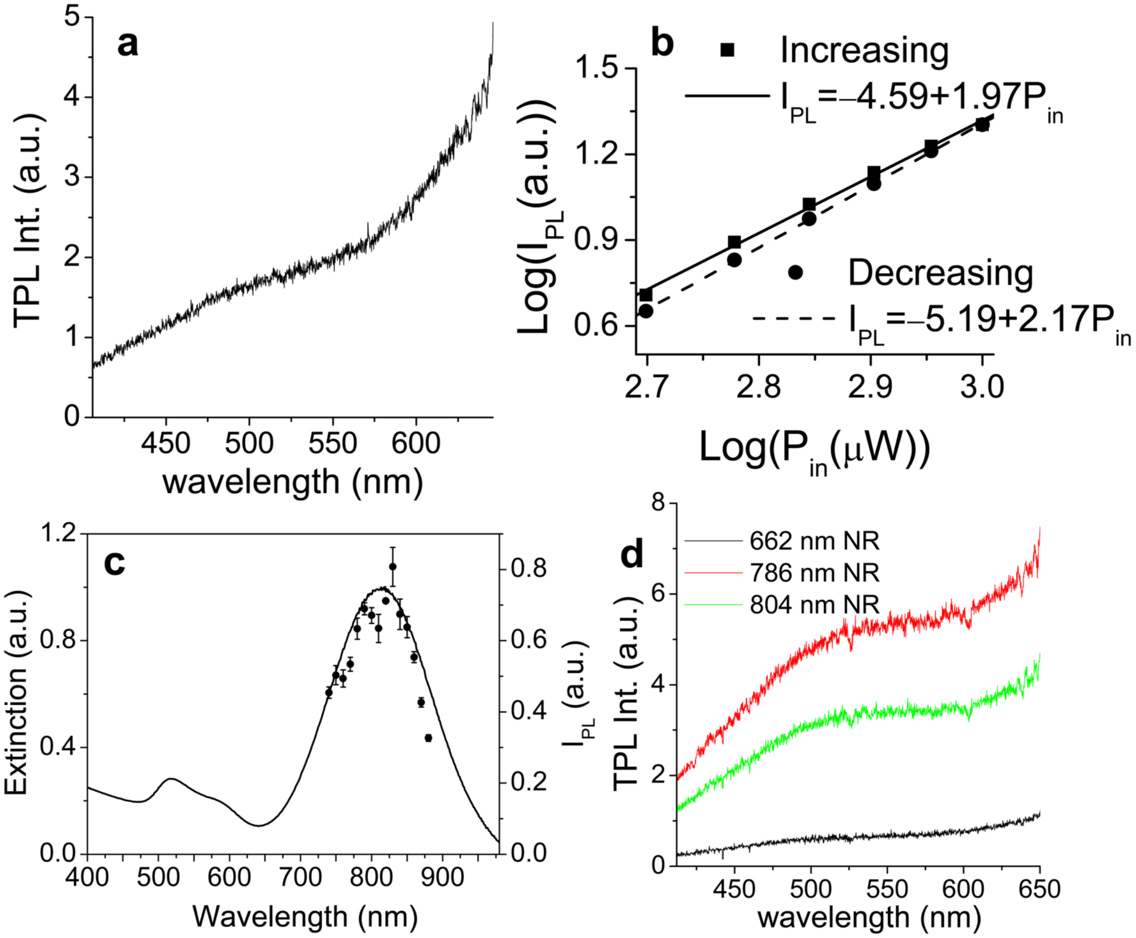

Figure 4. Characterization of TPL from gold NRs by far-field microscopy

(a) A typical TPL spectrum from a single NR excited by fs-pulsed laser centered at its LPR peak at 786 nm. The laser power was 1.5 mW and acquisition time was 1 s. The spectrum was cut off at 650 nm by an IR blocker. (b) Quadratic dependence of TPL emission intensity on excitation power. The data were obtained by increasing the excitation pulse energy from 1 to 2 pJ, then decreasing the power accordingly. Signal intensities were integrated over an area of 250 × 250 μm (18). (c) TPL excitation spectrum (circles with error bars, right y-axis) compared with NR extinction. The peak at 820 nm corresponds to the longitudinal plasmon mode. The same power (0.17 mW) was used for all excitation wavelengths (18). (d) TPL spectra of three NR solutions with resonance peaks at 660 nm (black line), 786 nm (red line), and 804 nm (green line), irradiated by the same excitation laser (785 nm, 3 mW; acquisition time 60 s). TPL spectra were cut off at 650 nm by an IR blocker.

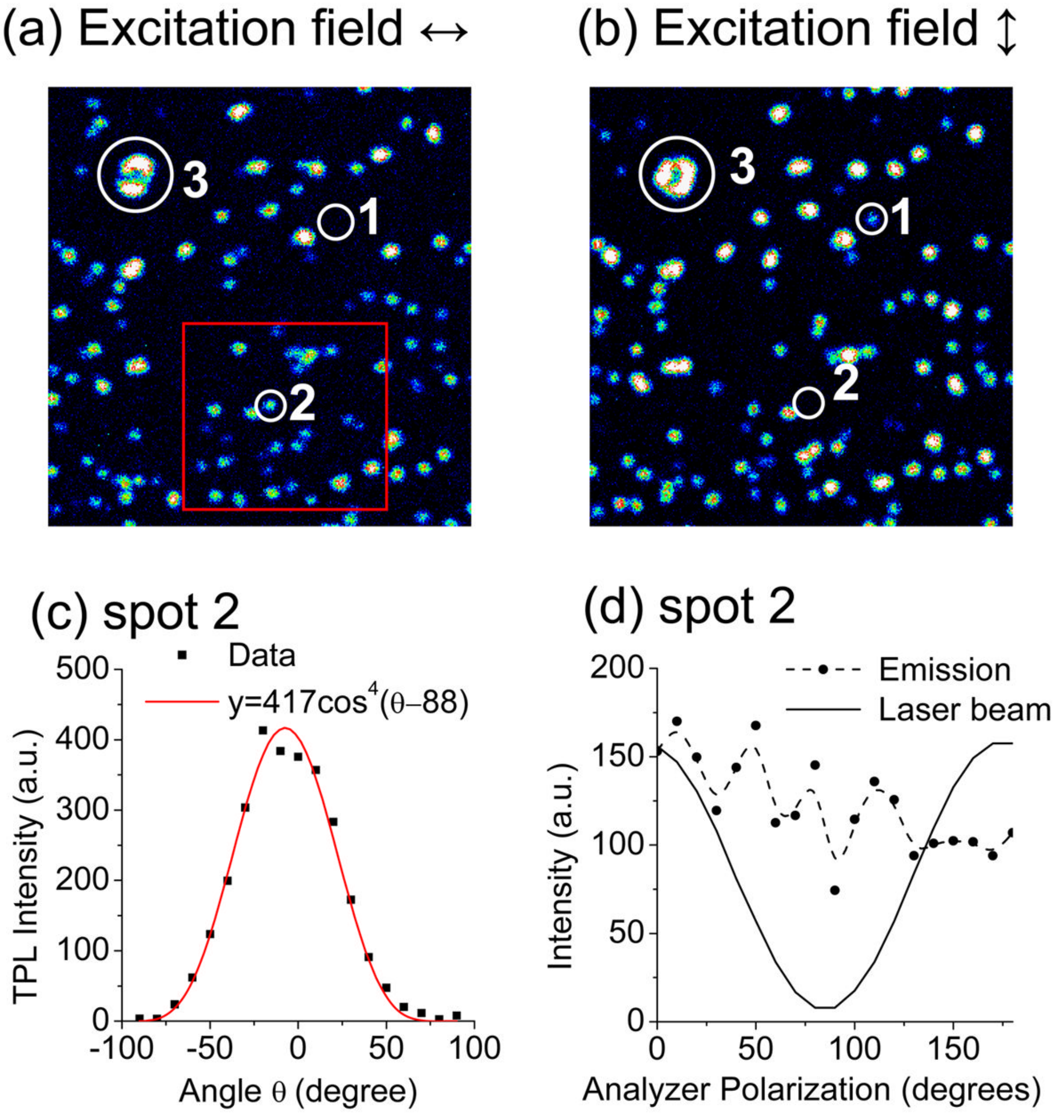

Figure 5. Polarization-dependent TPL intensities of gold NRs

(18). (a,b) Pseudocolor images with horizontal (θ=0°) and vertical (θ=90°) excitation polarizations, respectively. Single NRs could be identified by their similar range of intensities (e.g. spots 1, 2); brighter spots were considered to be clusters of NRs (e.g. spot 3). (b) Polarization dependence of the TPL intensity (solid dots) for a single NR (spot 2). The excitation polarization was rotated clockwise from −90° to +90° in 10° increments. The TPL signal fits a $\cos^4$ function, offset by 6.8° (red curve). (d) The TPL emission (solid dots) from the same NR (spot 2) measured by rotating a polarizer before the detector. The reflected excitation beam was linearly polarized at the detector site (solid curve), but the TPL emission was essentially depolarized.

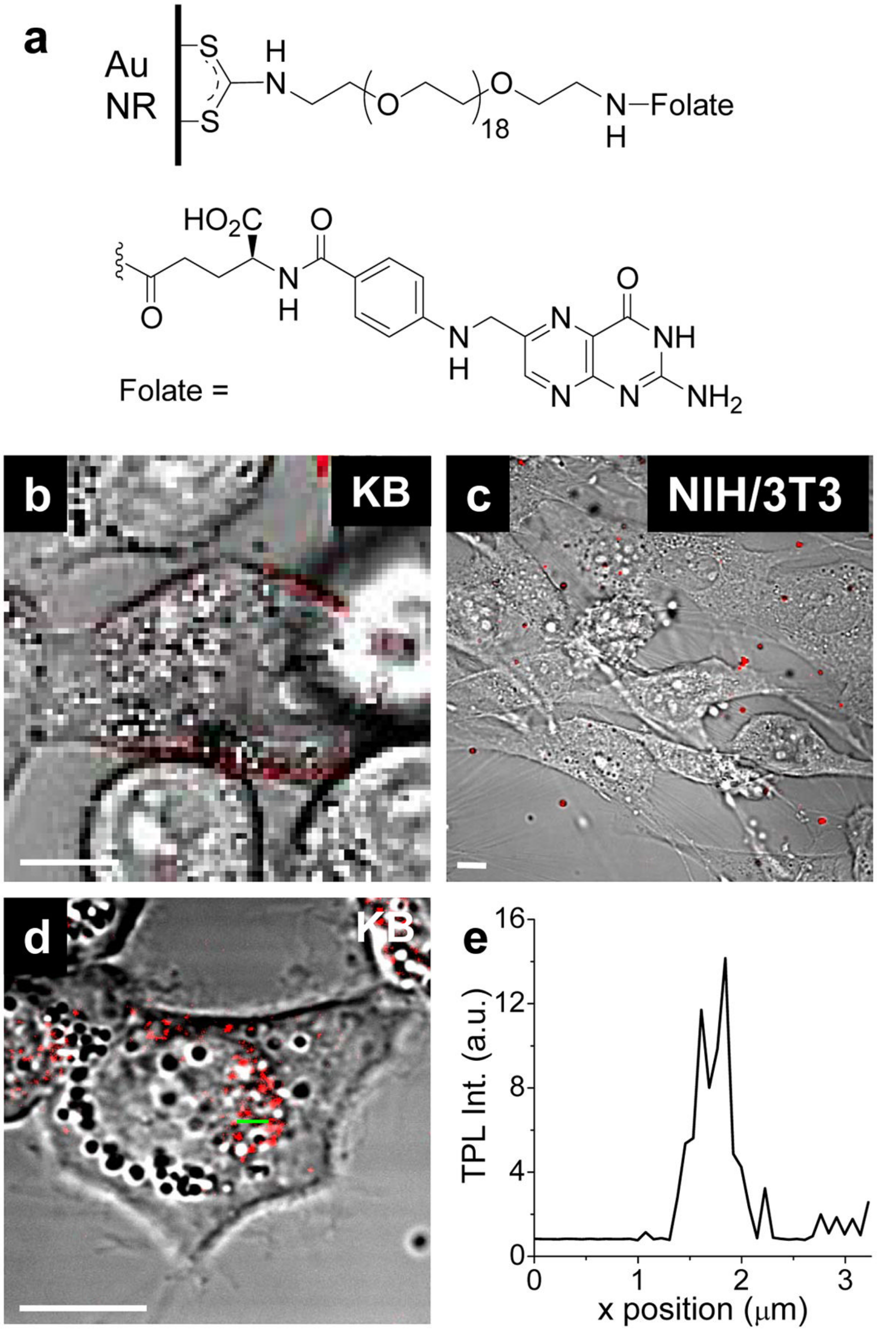

Figure 6. *In vitro* cellular imaging with F-NRs (34)

(a) folate-oligoethyleneglycol ligands, conjugated onto NR surface by *in situ* dithiocarbamate formation. (b) F-NRs bound to the KB cell surface after incubation for 6 hours. (c) Almost no F-NRs were observed to be associated with NIH/3T3 cells, which do not overexpress the high-affinity folate receptor. (d) F-NRs were internalized into KB cells and delivered to the perinuclear area after incubation for 17 hours. (e) TPL intensity profile across green line in (d). Bar= 10 μm.

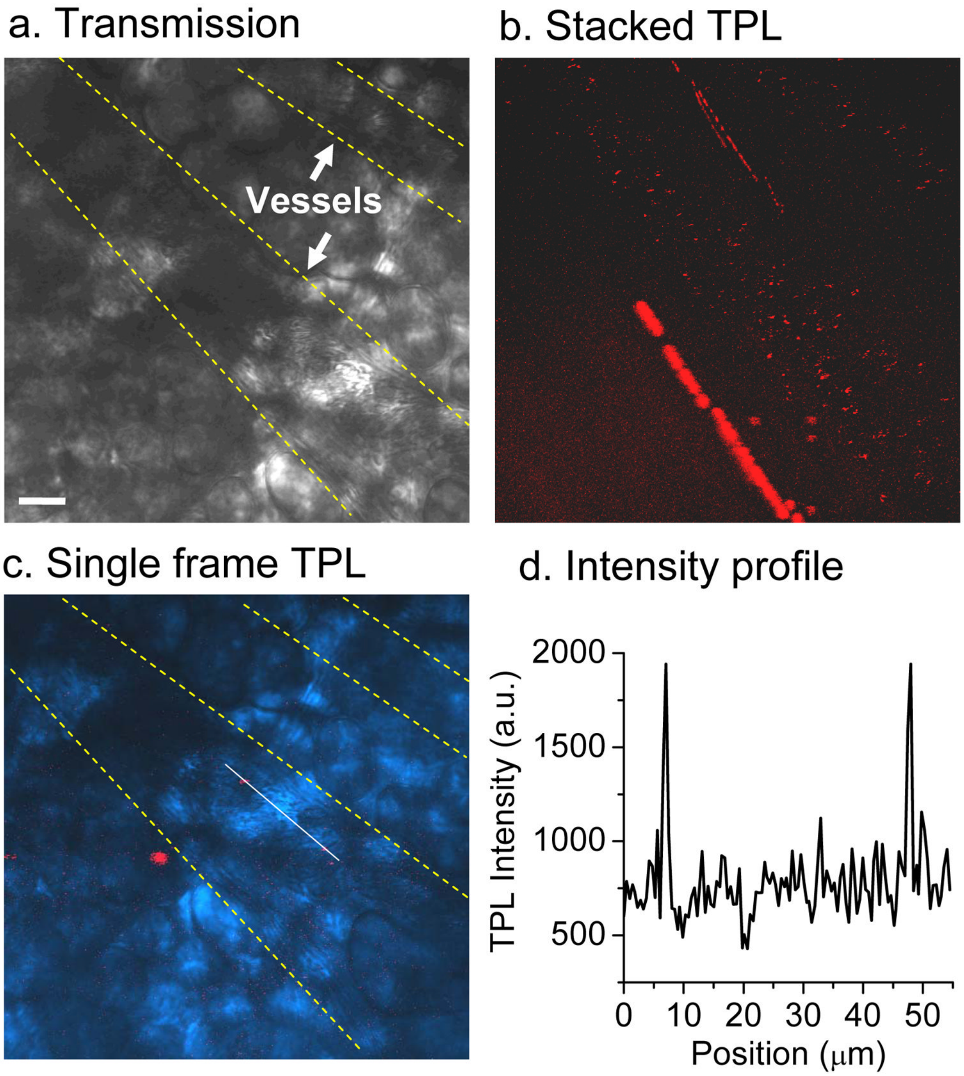

Figure 7. *In vivo* TPL imaging of NRs in blood vessels

(18). (a) Transmission image with two blood vessels indicated. (b) TPL image of CTAB-NRs (red dots) flowing through blood vessels. The image was compiled by stacking 300 frames collected continuously at a rate of 1.12 s per frame. (c) Overlay of transmission image (blue) and a single-frame TPL image. Two NRs (red) are superimposed by a linescan. (d) TPL intensity profile from the linescan in (c). Bar = 20 μm.

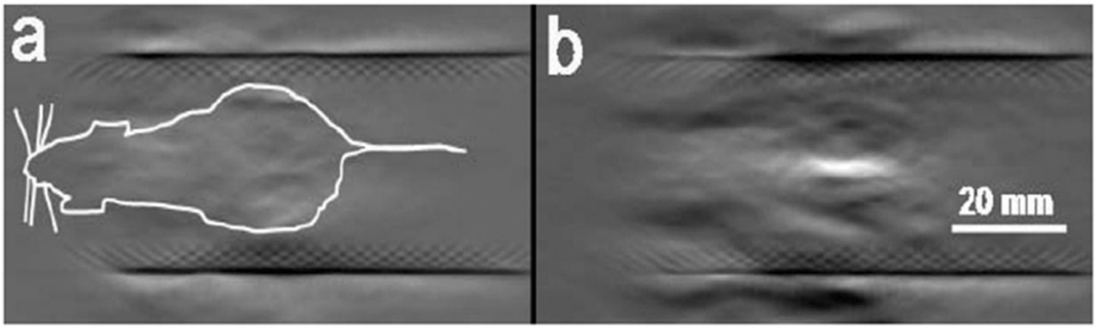

Figure 8. NRs as contrast agents for photoacoustic tomography

(88). (a) PAT image of a nude mouse (white outline) prior to injection of NRs; (b) PAT contrast after NR injection. Reprinted with permission from the American Chemical Society.

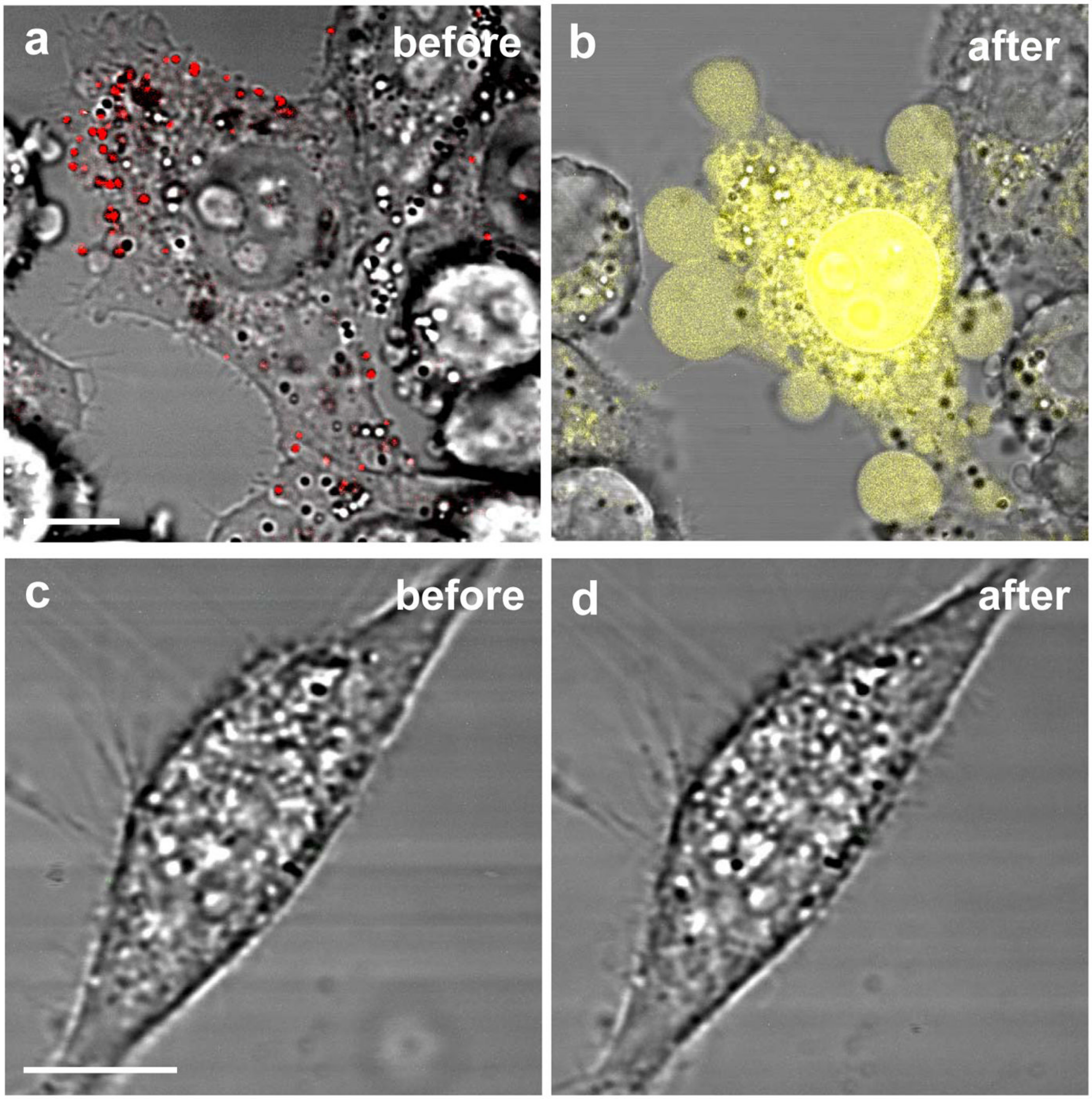

Figure 9. Photothermolysis mediated by F-NRs

(34). (a,b) KB cells with membrane-bound F-NRs (red) exposed to fs-pulsed NIR laser irradiation (0.75 mW, 81.4 s) experienced membrane damage and blebbing. The loss of membrane integrity was indicated by ethidium bromide (EB) nuclear staining (yellow). (c,d) NIH-3T3 cells were unresponsive to F-NRs and did not suffer photoinduced damage at the same condition. Bar= 10 μm.

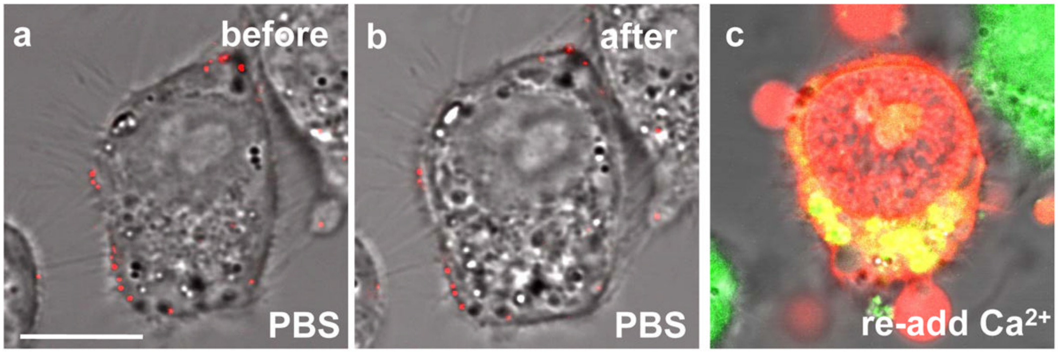

Figure 10. Ca^{2+}-dependent membrane blebbing during nanorod-mediated photothermolysis (34)
(a–b) No blebbing was observed for F-NRs labeled KB cells in Ca^{2+}-free PBS after fs-pulsed laser irradiation at 3 mW for 61.5 s. (c) Blebs were immediately produced upon addition of 0.9 mM Ca^{2+}. Incubation with 2.5 μM EB (red) and 2 μM Oregon Green for 20 min indicated a compromise in membrane integrity and an elevation in intracellular Ca^{2+}. For all experiments, cells were incubated with F-NRs for 6 h, and washed 5 times in Ca^{2+}-free PBS. Amounts of dyes and reagents were described as final concentrations in the cell culture medium. Bar = 10 μm.